THE JOURNAL OF PHYSICAL CHEMISTRY LETTERS
A JOURNAL OF THE AMERICAN CHEMICAL SOCIETY

pubs.acs.org/JPCL

Letter

Room-Temperature Continuous-Wave Microcavity Lasers from Solution-Processed Smooth Quasi-2D Perovskite Films with Low Thresholds

Xiang Gao, Jie Lin, Xiaoyang Guo, Geng He, Deyue Zou, Tomohiro Ishii, Dezhong Zhang, Chenyang Zhao, Hongmei Zhan, Jing Song Huang, Xingyuan Liu,* Chihaya Adachi, Chuanjiang Qin,* and Lixiang Wang

Cite This: *J. Phys. Chem. Lett.* 2023, 14, 2493−2500

Read Online

ACCESS | Metrics & More | Article Recommendations | Supporting Information

ABSTRACT: Continuous-wave (CW) lasing in quasi-two-dimensional (2D) perovskite-based distributed feedback cavities has been achieved at room temperature; however, CW microcavity lasers comprising distributed Bragg reflectors (DBRs) have rarely been prepared using solution-processed quasi-2D perovskite films because the roughness of perovskite films significantly increases intersurface scattering loss in the microcavity. Herein, high-quality spin-coated quasi-2D perovskite gain films were prepared using an antisolvent to reduce roughness. The highly reflective top DBR mirrors were deposited via room-temperature e-beam evaporation to protect the perovskite gain layer. Lasing emission of the prepared quasi-2D perovskite microcavity lasers under CW optical pumping was clearly observed at room temperature, featuring a low threshold of ∼1.4 W cm^{-2} and beam divergence of ∼3.5°. It was concluded that these lasers originated from weakly coupled excitons. These results elucidate the importance of controlling the roughness of quasi-2D films to achieve CW lasing, thus facilitating the design of electrically pumped perovskite microcavity lasers.

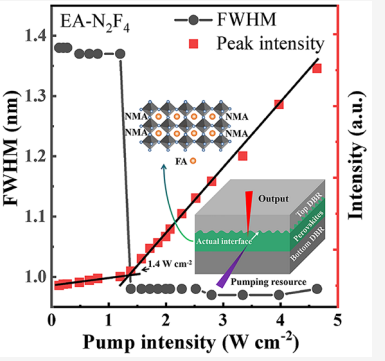

Quasi-two-dimensional (quasi-2D) organic-inorganic lead halide perovskites have received considerable attention in the field of optoelectronics because of their excellent photophysical properties, low cost, and solution processability.[1−7] By virtue of their quantum well structure and the high dielectric constant of large organic cations, quasi-2D perovskites possess high exciton binding energies, high gain coefficients, and a strong exciton confinement property.[8,9] These features make them suitable for use as optical gain media in lasing applications.[10−12] Recently, continuous-wave (CW) lasing was reported in a quasi-2D perovskite-based distributed feedback (DFB) cavity at room temperature through the suppression of singlet-triplet exciton annihilation by oxygen or organic cations with low triplet energies.[13] This is a critical step for fabricating electrical pumping lasers.[14−16]

Microcavities are widely used to fabricate vertical-cavity surface-emitting lasers (VCSELs), which can be integrated with silicon-based optoelectronic devices for broader applications.[17−19] Distributed Bragg reflectors (DBRs) are microcavity mirrors used to provide feedback for light amplification.[20−24] Considering the soft-matter nature of quasi-2D perovskites, room-temperature e-beam evaporation can be used to suppress the destruction of perovskite gain layers when fabricating top DBR mirrors.[25−27] However, lasing of CW DBR microcavities with quasi-2D perovskite films is rarely explored at room temperature due to the lack of material optimization and high-quality cavity construction. The threshold value of laser devices is significantly influenced by the interface state between the perovskite gain layer and DBR mirrors as well as by the additional optical loss generated when fabricating the top DBR mirrors.[21,28,29] The intersurface scattering loss in the optical loss of laser reflectors can have a fatal influence on the performance and testing of laser devices.[30,31] For instance, the $(PEA)_2PbI_4$ CW DBR laser comprises single-crystalline perovskites with high surface roughness, which leads to high thresholds.[32] Therefore, an understanding of the intersurface scattering loss and a reduction in the surface roughness of quasi-2D perovskite films in such devices are essential for achieving CW DBR microcavity lasing. In addition, fabricating top DBR mirrors on perovskite films is technically challenging.[33,34]

Herein, we prepared room-temperature CW microcavity lasers using a solution-processed quasi-2D perovskite $(NMA)_2FA_4Pb_5Br_{16}$ (NMA, 1-naphthylmethylamine; FA, formamidinium, N_2F_4) thin film with ultralow gain thresholds. Compared with the N_2F_4 films based on the antisolvent

Received: January 31, 2023
Accepted: March 1, 2023
Published: March 3, 2023

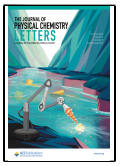

https://doi.org/10.1021/acs.jpclett.3c00279
J. Phys. Chem. Lett. 2023, 14, 2493−2500

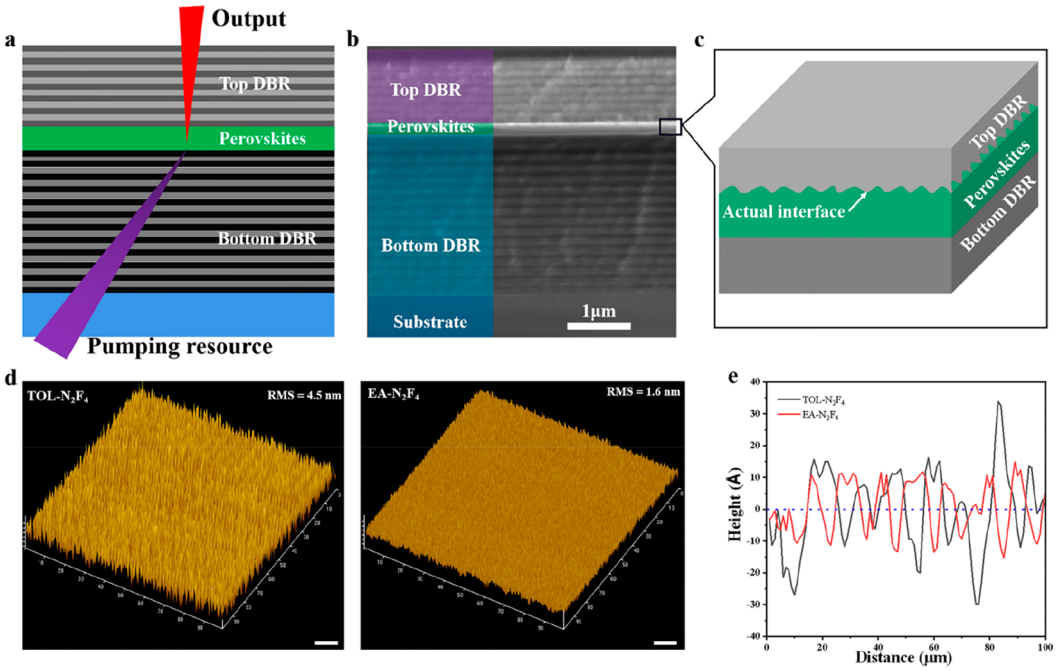

Figure 1. Schematic representation of the laser device and surface properties of N_2F_4 films. (a) The ideal schematic of the laser device. (b) Cross-sectional scanning electron microscopy (SEM) image of the actual device. (c) The actual schematic of the interface between the perovskite gain layer and top DBR. (d) Atomic force microscopy image of the TOL-N_2F_4 and EA-N_2F_4 films. The horizontal scale bar is 10 μm. (e) Corresponding height profile of the TOL-N_2F_4 and EA-N_2F_4 films at the 100 microscale.

toluene (TOL-N_2F_4), the N_2F_4 films based on the antisolvent ethyl acetate (EA) (EA-N_2F_4) significantly reduced the roughness of the N_2F_4 films and the intersurface scattering loss between the N_2F_4 gain layer and top DBR. The top DBR with high reflectivity was prepared on the N_2F_4 films directly via room-temperature e-beam evaporation. The threshold and full width at half-maximum (fwhm) are further reduced by virtue of the smoother EA-N_2F_4 gain layer in the DBR cavity. A clear lasing emission in quasi-2D perovskite N_2F_4-based microcavity lasers was observed under CW optical pumping, exhibiting an ultralow threshold of ~1.4 W cm^{-2} and a beam divergence of ~3.5°. Our findings offer a valuable strategy for the realization of electrically pumped perovskite lasers.

A schematic of the microcavity laser is shown in Figure 1a. The device comprised a bottom DBR, gain layer, and top DBR. We confirmed the optimum DBR parameters using the transfer matrix method and designed the bottom and top DBRs to satisfy all requirements of microcavity lasers.[35] In the DBR structure, the vertical-cavity mode governs the emission wavelength of the laser, with the resonance condition satisfying eq 1:

$$\frac{2\pi}{\lambda}\sum_i 2n_i d_i - (\varphi_1 + \varphi_2) = 2m\pi \tag{1}$$

The wavelength λ of the cavity modes is determined using the Fabry−Perot condition,[36] where φ_1 and φ_2 are the phase changes caused by the reflection from the two mirrors; n_i and d_i are the refractive indices and thicknesses of the cavity layers, respectively; and m is an integer.[37]

The top DBR, which comprised 8.5 pairs of alternating ZnS (2.38/60.8 nm) and MgF_2 (1.48/86.6 nm) layers with different refractive indices, has been prepared using room-temperature e-beam evaporation. This method is believed to be less destructive to the thin-film perovskite layers, which can effectively reduce the additional optical loss generated during the preparation of the top DBR mirror.[38] The bottom DBR, which comprised 15.5 pairs of alternating TiO_2 (2.36/62.5 nm) and SiO_2 (1.46/88.9 nm) layers with different refractive indices, was obtained using high-temperature e-beam evaporation. The high-reflectivity stop band of this DBR is very wide; that is, the stop band of the bottom and top DBRs is larger than 150 and 120 nm, respectively (Figure S1). In the resonance condition of optical microcavity ($2(\sum n_i d_i + L_{DBR1} + L_{DBR2}) = m\lambda$), resonance wavelength is related to material thickness and refractive index. Because the dielectric DBR has a wider high-reflection stop band that is much larger than the spectral line width of the perovskite in actual experiments, the thickness of the perovskites does not strictly match the Bragg center wavelength of the DBR and the intrinsic luminescence peak of the material; however, the microcavity resonance mode is consistent.

An ideal cavity confines light indefinitely (without loss). The quality factor (Q factor) of the resonant cavity is determined as follows:

$$Q = \frac{\lambda}{\Delta\lambda} = \frac{2\pi}{\lambda}\frac{2nL}{\ln(R_1R_2)^{-1}} \tag{2}$$

where L is the effective length of the cavity; λ is the resonant wavelength; $\Delta\lambda$ is the fwhm;n is the effective refractive index of the microcavity; and R_1 and R_2 represent the reflectance of the bottom and top DBRs, respectively. In our microcavity lasers, the theoretical reflectance of the bottom and top DBRs exceeds 99.999 and 99.92% between 460 and 590 nm, respectively (Figure S1). Therefore, this microcavity can exhibit extremely high Q values and a very low fwhm. However, all microcavities experience losses due to unsmooth contact surfaces. Figure 1b presents the cross-sectional image of the prepared microcavity by using scanning electron

https://doi.org/10.1021/acs.jpclett.3c00279
J. Phys. Chem. Lett. 2023, 14, 2493−2500

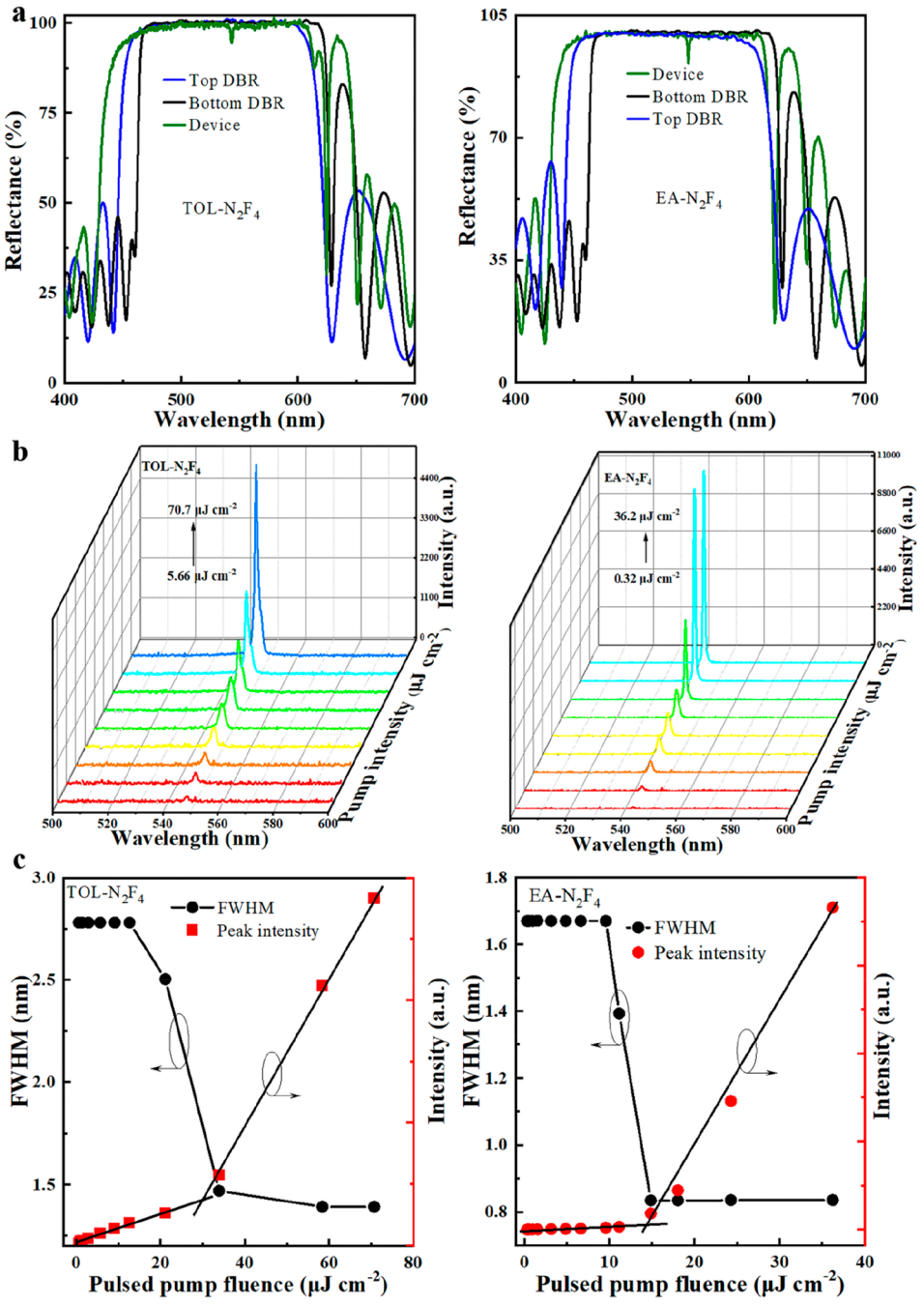

Figure 2. Pulsed lasing properties of TOL-N_2F_4 and EA-N_2F_4 microcavity lasers. (a) Reflectance spectra of DBRs with the TOL-N_2F_4 and EA-N_2F_4 films. (b) Spectrum evolution under different pulsed pump fluences of the TOL-N_2F_4 and EA-N_2F_4 devices. (c) Integrated PL intensity and fwhm as a function of the pulsed pump fluence of the TOL-N_2F_4 and EA-N_2F_4 devices, yielding threshold pump fluences of 29 and 14 μJ cm^{-2}, respectively.

microscopy (SEM). A clear multilayer structure of the bottom and top DBRs can be observed along with a perovskite gain layer. A schematic of the interface between the perovskite gain layer and top DBR is shown in Figure 1c. A rougher perovskite surface has a significant impact on the interface state between the perovskite gain layer and DBR mirrors, which increases the intersurface scattering loss and makes it difficult to fabricate a CW laser. The intersurface scattering loss can be represented as total integrated scattering (TIS):[39]

$$\mathrm{TIS} = 1 - \exp^{[-(4\pi\delta\cos\theta_0/\lambda)^2]} \quad (3)$$

where θ_0 is the angle of incidence and δ is the surface roughness of the perovskite films. For perovskite films, TIS can be simply related to the root-mean-square (RMS) roughness.

Based on our previous reports,[13,40] we selected brighter solution-processed N_2F_4 films as gain media (PLQY ≈ 90%) instead of quasi-2D perovskite N_2F_8 films (PLQY ≈ 70%), as shown in Figures S2 and S3. The typical atomic model for N_2F_4 is depicted in Figure S4. We prepared N_2F_4 films with the antisolvents TOL and EA by using a one-step spin-coating method under nitrogen conditions. EA-N_2F_4 and TOL-N_2F_4 films with the same thickness have the same refractive index

https://doi.org/10.1021/acs.jpclett.3c00279
J. Phys. Chem. Lett. 2023, 14, 2493−2500

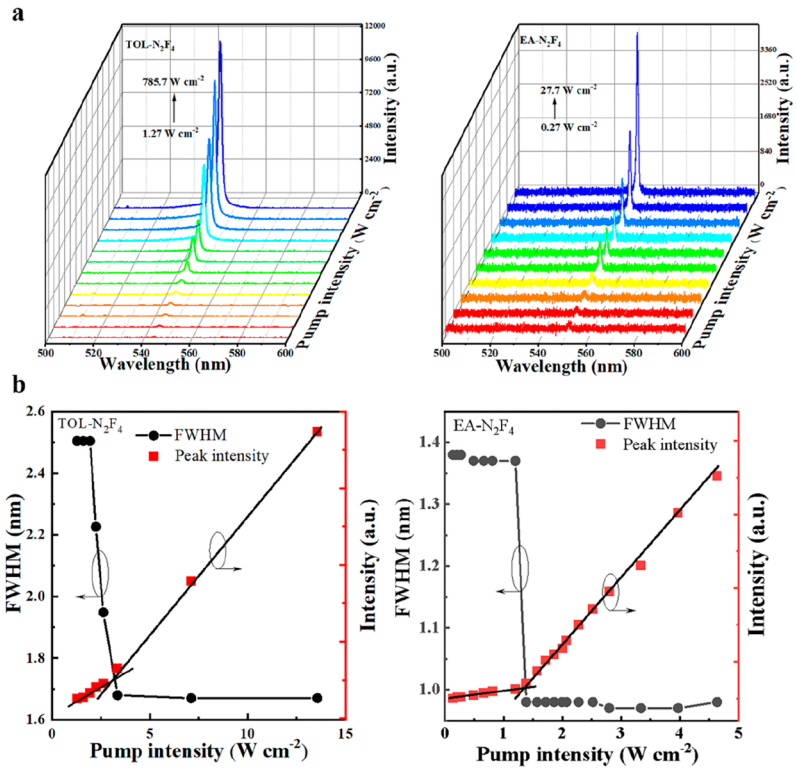

Figure 3. CW lasing characteristics of TOL-N_2F_4 and EA-N_2F_4 microcavity lasers. (a) Evolution of emission spectra under CW excitation at different pump intensities of the TOL-N_2F_4 and EA-N_2F_4 devices. (b) Emission intensity and fwhm as a function of the pump intensity of the TOL-N_2F_4 and EA-N_2F_4 devices, yielding threshold power densities of 3.0 and 1.4 W cm^{-2}, respectively.

(~2.14 at 550 nm; Figure S5); EA-N_2F_4 films have similar optical properties and crystal structures to those of TOL-N_2F_4 films (Figures S6 and S7). The photoluminescence (PL) spectra of the two N_2F_4 films show a luminescence peak at ~536 nm and an fwhm of ~24 nm. The XRD patterns representing the crystal structure of the N_2F_4 films indicated that the crystalline skeleton inside perovskites is in the cubic phase, while grazing incidence X-ray diffraction (GIXRD) showed that these films have similar orientations (Figure S7).

Figure S8 shows that EA-N_2F_4 films exhibit better amplified spontaneous emission (ASE) performance than that of TOL-N_2F_4 films, including a 23% decrease in the ASE threshold (17 μJ cm^{-2}) and a 20% decrease in fwhm (2.0 nm). The low threshold characteristics suggest that N_2F_4 is a promising gain medium for the resonant cavity laser.[41−44] We attempted to achieve ASE under CW excitation on N_2F_4 perovskite films deposited on different quartz or Si/SiO_2 substrates. Unfortunately, we were unable to obtain ASE under CW excitation at room temperature in air. The commonly used method for testing the ASE profile of thin films involves a planar waveguide structure that provides optical feedback. Although simple in structure and useful for measuring the gain of thin-film materials, this method is not perfect and represents a significant source of loss in optical waveguides.[45] Therefore, achieving CW pumped ASE at room temperature from quasi-2D perovskite films remains challenging. In addition to the ASE threshold, the optical gain coefficient (g) is also a key characteristic of perovskite gain media. The optical gain of the N_2F_4 film was determined using the variable stripe length (VSL) method.[46] As Figure S9 shows, gain coefficients of 280 and 305 cm^{-1} were obtained for samples TOL-N_2F_4 and EA-N_2F_4 respectively, which are comparable to traditional quasi-2D perovskites and better than some of the 3D perovskites.[33,47] The difference in ASE performance is attributed to the RMS roughness and PLQY between the TOL-N_2F_4 and EA-N_2F_4 films. On the one hand, ASE performance is closely related to the PL properties. EA-N_2F_4 film has a higher PLQY than TOL-N_2F_4 film, as shown in Figures S2 and S3. On the other hand, the perovskite layer requires high surface coverage and low roughness to achieve high-performance ASE and lasers; as shown in Figure 1d, atomic force microscopy (AFM) clarified that the EA-N_2F_4 film exhibits low roughness and high coverage on the bottom DBR. The RMS roughness of the EA-N_2F_4 film (RMS ≈ 1.5 nm) is lower than that of the TOL-N_2F_4 film (RMS ≈ 4.5 nm). Meanwhile, as shown in Figure S10, the EA-N_2F_4 film exhibits a more complete densified and uniform grain size on the bottom DBR than the TOL-N_2F_4 film. Analysis of eq 3 reveals that lower roughness can reduce the intersurface scattering loss between the EA-N_2F_4 films and top DBR. The corresponding height profile of the TOL-N_2F_4 and EA-N_2F_4 films at the 100 microscale demonstrated that the smoother EA-N_2F_4 films display superior microscopic flatness than that of TOL-N_2F_4 films (Figure 1e). Thus, EA-N_2F_4 films with low RMS roughness and excellent microscopic flatness have better potential for lasing.

The laser devices were tested at room temperature under pulse excitation (Nd:YAG laser, 355 nm, pulse width 10 ns, 1 kHz). A schematic of the laser pump setup is depicted in Figure S11, and photo images of TOL-N_2F_4 and EA-N_2F_4 VCSEL devices under white light illumination are shown in Figure S12. Figure S13 presents the magnified cross section images of the prepared N_2F_4 laser devices by SEM. A clear multilayer structure of bottom and top DBRs and a perovskite gain layer could be observed. The smooth interface between

https://doi.org/10.1021/acs.jpclett.3c00279
J. Phys. Chem. Lett. 2023, 14, 2493−2500

Table 1. Lasing Threshold Comparison for Perovskite Microcavity Lasers at Room Temperature

Materials	Morphology	Synthesis of Perovskites	Fabrication of DBR cavities	Pump laser	Wavelength [nm]	Threshold	Q-factor	Ref
$MAPbI_3$	Film	Spin-coating	Manually laminating	pulsed	778	7.6 μJ cm^{-2}	1100	22
$FAPbBr_3$	Film	Spin-coating	Sputtering	pulsed	552.4	~18.3 μJ cm^{-2}	1420	48
$Cs_{0.17}FA_{0.83}PbBr_3$	Film	Spin-coating	Sputtering	pulsed	552.6	13.5 μJ cm^{-2}	1350	31
OC-$CsPbBr_3$	Film	Co-evaporation	Manually laminating	pulsed	542	1.7 μJ cm^{-2}	NA	25
$CsPbBr_3$	Film	Thermal nanoimprint	Hot pressing	pulsed	538	2.2 μJ cm^{-2}	NA	49
$(PEA)_2Cs_{n-1}Pb_nBr_{3n+1}$	Microcrystals	Spin-coating	Evaporation of Ag	pulsed	532	500 μJ cm^{-2}	665	50
$MAPbCl_3$	Single crystal	In situ grown method	Manually laminating	pulsed	414–435	211 μJ cm^{-2}	1100	51
$MAPbBr_3$	Single-crystal film	In situ grown method	Manually laminating	pulsed	567	4 μJ cm^{-2}	810	29
$NMA_2FA_4Pb_5Br_{16}$	Film	Spin-coating	Room-temperature e-beam evaporation	pulsed	544	14 μJ cm^{-2}	688	This work
$MAPbBr_3$	Film	Vapor deposition	PECVD	CW	541	89 kW cm^{-2}	203	19
$MAPbBr_3$	Single-crystal film	In situ grown method	Manually laminating	CW	565	34 mW cm^{-2}	706	29
$(PEA)_2PbI_4$	Single crystal	Exfoliation	Low temperature e-beam evaporation	CW	537	5.7 W cm^{-2}	1194	32
$NMA_2FA_4Pb_5Br_{16}$	Film	Spin-coating	Room-temperature e-beam evaporation	CW	550	1.4 W cm^{-2}	568	This work

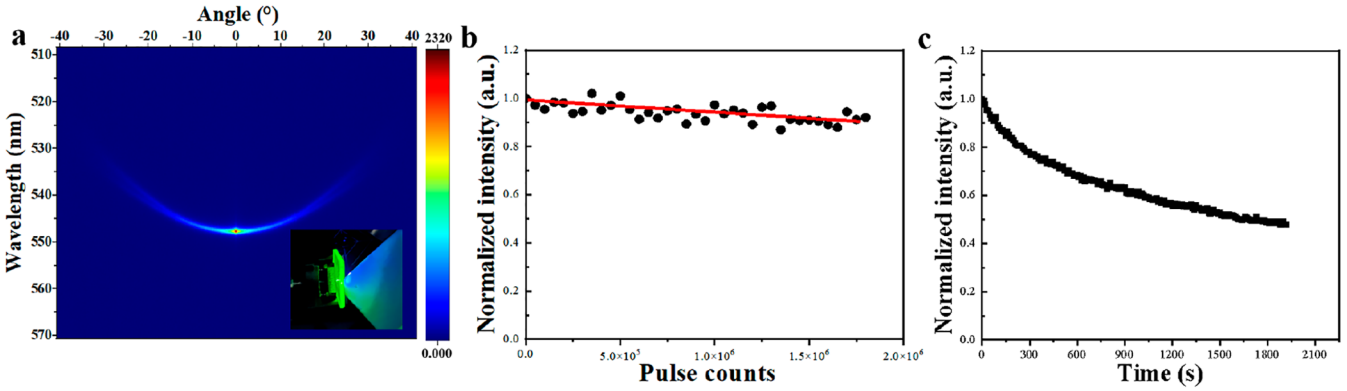

Figure 4. Spatial distribution of the output emission and stability characterizations of the EA-N_2F_4 microcavity laser. (a) Spatial distribution of the output emission via angle-resolved PL under CW excitation. Inset: Photograph of the far-field pattern of CW lasing. (b) Stability characterizations of the EA-N_2F_4 device under continuous pulse pumping, with pump fluence set at 1.5 Pulse P_{th}. (c) Operational stability of the EA-N_2F_4 device under CW excitation, with a pump intensity of 1.5 CW P_{th}.

the stacked layers indicated the high quality of the prepared microcavity and the low optical loss. As expected, the cavity mode of the EA-N_2F_4 device was more evident at ~550 nm compared to that of the TOL-N_2F_4 device (Figure 2a) because the smoother EA-N_2F_4 film leads to lower optical losses and is better matched with the high-level microcavity. The lasing wavelengths of TOL-N_2F_4 and EA-N_2F_4 devices appeared at either 546 or 544 nm, as shown in Figure 2b. Following an increase in the excitation intensity, the optical input and output behaviors are characterized by the change from a broad spontaneous emission to a narrow stimulated emission. Figure 2c shows that the threshold of the EA-N_2F_4 device is observed at 14 μJ cm^{-2} under pulse pumping, which is lower than that of the TOL-N_2F_4 device (29 μJ cm^{-2}). This can be attributed to the smoother EA-N_2F_4 surface reducing the intersurface scattering loss at the interface, which also validates the importance of introducing the antisolvent EA. Above the threshold, fwhm's of the TOL-N_2F_4 and EA-N_2F_4 devices at 546 and 544 nm are 2.6−1.4 and 1.7−0.82 nm, with reducing ratios of 46 and 52%, respectively. The Q factor of the EA-N_2F_4 device is ~688, which is about twice than that of the TOL-N_2F_4 device (392).

To investigate the CW lasing properties of the two devices, the devices were optically pumped at room temperature with a 405 nm CW laser source (405 nm, OBIS LX). A schematic of the CW optical pumping setup is depicted in Figure S14. The detailed pump-intensity-dependent lasing spectra of the TOL-N_2F_4 and EA-N_2F_4 devices are given in Figure 3a. The lasing peaks of the TOL-N_2F_4 and EA-N_2F_4 devices are centered at 545 and 550 nm, respectively. The slight shift of the lasing spectrum may be associated with the microscopic flatness of pump area on the devices. Figure 3b represents the lasing properties of the TOL-N_2F_4 and EA-N_2F_4 devices, and clear thresholds can be observed at 3.0 and 1.4 W cm^{-2} under CW pumping, respectively. The lasing emission fwhm for the TOL-N_2F_4 and EA-N_2F_4 devices is 1.65 and 0.97 nm, respectively. This CW lasing threshold is not only lower among the single-crystal 2D layered perovskite DBR lasers but also comparable with other high-performance perovskite planar microcavity devices (Table 1). There are several reasons for the low thresholds of our microcavity devices. First, the optimized

https://doi.org/10.1021/acs.jpclett.3c00279
J. Phys. Chem. Lett. 2023, 14, 2493−2500

N_2F_4 film has lower RMS roughness, thereby yielding excellent film flatness. Second, a microcavity with a high Q value and low optical loss can be constructed using the two DBRs through theoretical optimization of the structural design of the device. Most importantly, the optimized preparation process of the DBR as well as the direct deposition of the top DBR at room temperature on a high-quality N_2F_4 film may reduce the optical loss.

To characterize the laser beam quality, Figure 4a shows the spatial distribution of the output emission that indicates a small beam divergence when compared to the emission of our EA-N_2F_4 device (~3.5° divergence in the transverse plane). This angular divergence across the transverse plane is much smaller than that of the theoretical simulation (Figure S15). The inset of Figure 4a shows a photograph of the far-field pattern of CW lasing. Beyond the lasing threshold, a circular spot of light appears on the white paper screen, and the coherence in space can be inferred from the optical image with a bright spot. These results indicate that the microcavity has a good interaction with the perovskite gain medium of EA-N_2F_4. Both transverse-electric (TE) and transverse-magnetic (TM) modes exist throughout the reflectance spectrum at different angles (Figure S16). The CW lasing of the EA-N_2F_4 device also shows linear transverse-electric polarization (Figure S17). To evaluate the stability of the EA-N_2F_4 microcavity laser under different pump conditions, we recorded the lasing output of the EA-N_2F_4 microcavity device under continuous pulse pumping and CW excitation. In each case, the pump level was set at 1.5 times the threshold. The results are summarized in Figure 4b,c. The device exhibits good stability under nanosecond pump pulses (T_{90} > 1.8 × 10^6 pump pulses). Under CW excitation (~1.5 P_{th}), the lasing intensity decreases to 78, 57, and 49% of its original value over 300, 1200, and 1800 s, respectively. The narrow line width and peak position observed during the testing period confirm the persistence of laser operation (Figure S18).

Finally, we discuss the lasing mechanism of our microcavity lasers. Figure 5a shows a contour map of the transverse-magnetic (TM) angle-resolved reflectance measured for the microcavity. The squares show the dip position identified on the reflectance spectra for each angle (Figure 5b). In the microcavity, these peaks are found to intersect around excitonic resonances of E_{ex} = 2.39 eV. This behavior indicates that the resonator is located in the weak coupling region rather than in the strong coupling region.

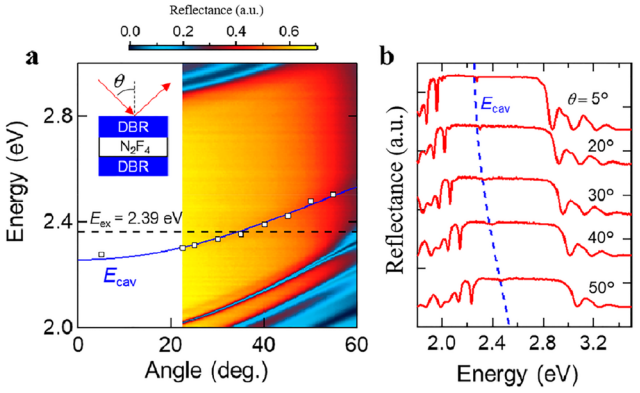

Figure 5. Angle-resolved reflectance curves of an EA-N_2F_4 device. (a) Contour maps of the angle-resolved reflectance for transverse-magnetic polarization of the microcavity. The positions of individual minima identified on the spectra are shown as white square dots for each angle (Figure 5b). The black dashed line shows the uncoupled exciton (E_{ex} = 2.39 eV). Additionally, the blue solid line shows the cavity photon dispersion obtained from eq 4 (inset: schematic of angle-resolved reflectance measurement). (b) Angle-resolved reflectance spectra of the microcavity.

To calculate the cavity photon dispersion for the obtained peaks, we simulated the curve using eq 4:

$$E_{ph}(\theta) = E_{ph}(0)\left(1 - \frac{\sin^2\theta}{n_{eff}^2}\right)^{-1/2} \quad (4)$$

where $E_{ph}(0)$ is the photon energy at θ = 0° and n_{eff} is the effective refractive index; these parameters were estimated to be E_{ph} (0) = 2.26 eV and n_{eff} = 1.9. Figure 5a shows that the curvature of the dispersion obtained by the simulation reproduces the experimental data well. This result strongly suggests that the cavity photon is not strongly coupled to excitons. Therefore, we concluded that the observed lasing in this study originates from photon lasing.[52]

In summary, by reducing the roughness of quasi-2D perovskite films, a continuous optically pumped microcavity laser with solution-processed N_2F_4 films was obtained under the air atmosphere at the room temperature. These perovskite N_2F_4 films, which exhibited low roughness and excellent microscopic flatness, were fabricated via a spin-coating method by using the antisolvent EA. Furthermore, highly reflective top DBR mirrors were prepared on the N_2F_4 films via room-temperature e-beam evaporation. The low-pulse ASE threshold (17 μJ cm^{-2}) at room temperature showed that N_2F_4 films exhibit good gain characteristics. Notably, by combining the excellent gain characteristics of the smooth N_2F_4 films with the optical constraint of DBR mirrors, a CW laser with an ultralow threshold of 1.4 W cm^{-2} and a beam divergence of ~3.5° was realized using the EA-N_2F_4 microcavity structure. This study demonstrates the strong potential of microcavity devices for future development of electrically pumped perovskite lasers in the future.

■ ASSOCIATED CONTENT

Supporting Information

The Supporting Information is available free of charge at https://pubs.acs.org/doi/10.1021/acs.jpclett.3c00279.

Experimental methods, structure of the quasi-2D perovskite, refractive index curve, ultraviolet−visible absorption, PLQY, PL, XRD pattern, GIXRD, SEM, ASE, and optical gain properties of the films; detailed evolution of emission spectra, theoretically simulated map, the polar plot of peak intensity versus the N_2F_4 devices; schematic diagram of pulsed optical pumping setup, reflectance spectra at different angles (PDF)

■ AUTHOR INFORMATION

Corresponding Authors

Chuanjiang Qin − *State Key Laboratory of Polymer Physics and Chemistry, Changchun Institute of Applied Chemistry, Chinese Academy of Sciences, Changchun 130022, P. R. China;* orcid.org/0000-0002-6927-2544; Email: cjqin@ciac.ac.cn

Xingyuan Liu − *State Key Laboratory of Luminescence and Applications, Changchun Institute of Optics, Fine Mechanics*

https://doi.org/10.1021/acs.jpclett.3c00279
J. Phys. Chem. Lett. 2023, 14, 2493−2500

and Physics, Chinese Academy of Sciences, Changchun 130033, P. R. China; orcid.org/0000-0002-9681-1646; Email: liuxy@ciomp.ac.cn

Authors

Xiang Gao − *State Key Laboratory of Polymer Physics and Chemistry, Changchun Institute of Applied Chemistry, Chinese Academy of Sciences, Changchun 130022, P. R. China*

Jie Lin − *Oxford Suzhou Centre for Advanced Research (OSCAR), University of Oxford, Suzhou 215123, P. R. China;* orcid.org/0000-0001-9676-2218

Xiaoyang Guo − *State Key Laboratory of Luminescence and Applications, Changchun Institute of Optics, Fine Mechanics and Physics, Chinese Academy of Sciences, Changchun 130033, P. R. China;* orcid.org/0000-0003-0259-137X

Geng He − *Oxford Suzhou Centre for Advanced Research (OSCAR), University of Oxford, Suzhou 215123, P. R. China*

Deyue Zou − *State Key Laboratory of Luminescence and Applications, Changchun Institute of Optics, Fine Mechanics and Physics, Chinese Academy of Sciences, Changchun 130033, P. R. China*

Tomohiro Ishii − *Center for Organic Photonics and Electronics Research (OPERA), Kyushu University, Nishi, Fukuoka 819-0395, Japan*

Dezhong Zhang − *State Key Laboratory of Polymer Physics and Chemistry, Changchun Institute of Applied Chemistry, Chinese Academy of Sciences, Changchun 130022, P. R. China*

Chenyang Zhao − *State Key Laboratory of Polymer Physics and Chemistry, Changchun Institute of Applied Chemistry, Chinese Academy of Sciences, Changchun 130022, P. R. China;* orcid.org/0000-0002-2100-580X

Hongmei Zhan − *State Key Laboratory of Polymer Physics and Chemistry, Changchun Institute of Applied Chemistry, Chinese Academy of Sciences, Changchun 130022, P. R. China;* orcid.org/0000-0001-5509-2457

Jing Song Huang − *Oxford Suzhou Centre for Advanced Research (OSCAR), University of Oxford, Suzhou 215123, P. R. China*

Chihaya Adachi − *Center for Organic Photonics and Electronics Research (OPERA), Kyushu University, Nishi, Fukuoka 819-0395, Japan;* orcid.org/0000-0001-6117-9604

Lixiang Wang − *State Key Laboratory of Polymer Physics and Chemistry, Changchun Institute of Applied Chemistry, Chinese Academy of Sciences, Changchun 130022, P. R. China;* orcid.org/0000-0002-4676-1927

Complete contact information is available at: https://pubs.acs.org/10.1021/acs.jpclett.3c00279

Notes

The authors declare no competing financial interest.

■ ACKNOWLEDGMENTS

X. Gao and J. Lin contributed equally to this work. The authors acknowledge financial support from National Key Research and Development program of China (No. 2019YFA0705900), the Perovskite Thin-Film Innovation Technology Centre (project number: YZCXPT2022104), and the Natural Science Foundation of China (Nos. 22075277, 61975256, 62035013, 51973208).

■ REFERENCES

(1) Zhou, N.; Shen, Y.; Li, L.; Tan, S.; Liu, N.; Zheng, G.; Chen, Q.; Zhou, H. The Exploration of Crystallization Kinetics in Quasi Two-Dimensional Perovskite and High Performance Solar Cells. *J. Am. Chem. Soc.* **2018**, *140*, 459.

(2) Xi, J.; Byeon, J.; Kim, U.; Bang, K.; Han, G. R.; Kim, J.-Y.; Yoon, J.; Dong, H.; Wu, Z.; Divitini, G.; et al. Abnormal Spatial Heterogeneity Governing the Charge-Carrier Mechanism in Efficient Ruddlesden−Popper Perovskite Solar Cells. *Energy & Energy Environ. Sci.* **2021**, *14*, 4915.

(3) Kong, L.; Zhang, X.; Li, Y.; Wang, H.; Jiang, Y.; Wang, S.; You, M.; Zhang, C.; Zhang, T.; Kershaw, S. V.; et al. Smoothing the Energy Transfer Pathway in Quasi-2d Perovskite Films Using Methanesulfonate Leads to Highly Efficient Light-Emitting Devices. *Nat. Commun.* **2021**, *12*, 1246.

(4) Guo, Z.; Zhang, Y.; Wang, B.; Wang, L.; Zhou, N.; Qiu, Z.; Li, N.; Chen, Y.; Zhu, C.; Xie, H.; et al. Promoting Energy Transfer Via Manipulation of Crystallization Kinetics of Quasi-2d Perovskites for Efficient Green Light-Emitting Diodes. *Adv. Mater.* **2021**, *33*, 2102246.

(5) Deschler, F.; Price, M.; Pathak, S.; Klintberg, L. E.; Jarausch, D.-D.; Higler, R.; Hüttner, S.; Leijtens, T.; Stranks, S. D.; Snaith, H. J.; et al. High Photoluminescence Efficiency and Optically Pumped Lasing in Solution-Processed Mixed Halide Perovskite Semiconductors. *J. Phys. Chem. Lett.* **2014**, *5*, 1421−1426.

(6) Nguyen, V.-C.; Katsuki, H.; Sasaki, F.; Yanagi, H. Optically Pumped Lasing in Single Crystals of Organometal Halide Perovskites Prepared by Cast-Capping Method. *Appl. Phys. Lett.* **2016**, *108*, 261105.

(7) Zhao, C.; Zhang, D.; Qin, C. Perovskite Light-Emitting Diodes. *CCS Chem.* **2020**, *2*, 859−869.

(8) Qin, C.; Matsushima, T.; Potscavage, W. J.; Sandanayaka, A. S. D.; Leyden, M. R.; Bencheikh, F.; Goushi, K.; Mathevet, F.; Heinrich, B.; Yumoto, G.; et al. Triplet Management for Efficient Perovskite Light-Emitting Diodes. *Nat. Photonics* **2020**, *14*, 70−75.

(9) Leyden, M. R.; Matsushima, T.; Qin, C.; Ruan, S.; Ye, H.; Adachi, C. Amplified Spontaneous Emission in Phenylethylammonium Methylammonium Lead Iodide Quasi-2d Perovskites. *Phys. Chem. Chem. Phys.* **2018**, *20*, 15030−15036.

(10) Zhang, H.; Liao, Q.; Wu, Y.; Zhang, Z.; Gao, Q.; Liu, P.; Li, M.; Yao, J.; Fu, H. 2d Ruddlesden−Popper Perovskites Microring Laser Array. *Adv. Mater.* **2018**, *30*, 1706186.

(11) Li, M.; Wei, Q.; Muduli, S. K.; Yantara, N.; Xu, Q.; Mathews, N.; Mhaisalkar, S. G.; Xing, G.; Sum, T. C. Enhanced Exciton and Photon Confinement in Ruddlesden−Popper Perovskite Microplatelets for Highly Stable Low-Threshold Polarized Lasing. *Adv. Mater.* **2018**, *30*, 1707235.

(12) Wang, R.; Tong, Y.; Manzi, A.; Wang, K.; Fu, Z.; Kentzinger, E.; Feldmann, J.; Urban, A. S.; Müller-Buschbaum, P.; Frielinghaus, H. Preferential Orientation of Crystals Induced by Incorporation of Organic Ligands in Mixed-Dimensional Hybrid Perovskite Films. *Adv. Opt. Mater.* **2018**, *6*, 1701311.

(13) Qin, C.; Sandanayaka, A. S. D.; Zhao, C.; Matsushima, T.; Zhang, D.; Fujihara, T.; Adachi, C. Stable Room-Temperature Continuous-Wave Lasing in Quasi-2d Perovskite Films. *Nature* **2020**, *585*, 53−57.

(14) Zhao, C.; Qin, C. Quasi-2d Lead Halide Perovskite Gain Materials toward Electrical Pumping Laser. *Nanophotonics* **2021**, *10*, 2167−2180.

(15) Dong, H.; Zhang, C.; Liu, X.; Yao, J.; Zhao, Y. S. Materials Chemistry and Engineering in Metal Halide Perovskite Lasers. *Chem. Soc. Rev.* **2020**, *49*, 951−982.

(16) Adachi, C.; Sandanayaka, A. S. D. The Leap from Organic Light-Emitting Diodes to Organic Semiconductor Laser Diodes. *CCS Chem.* **2020**, *2*, 1203−1216.

(17) Wang, J.; Su, R.; Xing, J.; Bao, D.; Diederichs, C.; Liu, S.; Liew, T. C.H.; Chen, Z.; Xiong, Q. Room Temperature Coherently Coupled Exciton Polaritons in Two-Dimensional Organic-Inorganic Perovskite. *ACS Nano* **2018**, *12*, 8382.

(18) Sun, W.; Liu, Y.; Qu, G.; Fan, Y.; Dai, W.; Wang, Y.; Song, Q.; Han, J.; Xiao, S. Lead Halide Perovskite Vortex Microlasers. *Nat. Commun.* **2020**, *11*, 4862.
(19) Alias, M. S.; Liu, Z.; Al-atawi, A.; Ng, T. K.; Wu, T.; Ooi, B. S. Continuous-Wave Optically Pumped Green Perovskite Vertical-Cavity Surface-Emitter. *Opt. Lett.* **2017**, *42*, 3618−3621.
(20) Wang, Y.; Li, X.; Nalla, V.; Zeng, H.; Sun, H. Solution-Processed Low Threshold Vertical Cavity Surface Emitting Lasers from All-Inorganic Perovskite Nanocrystals. *Adv. Funct. Mater.* **2017**, *27*, 1605088.
(21) Li, X.; Liu, W.; Song, Y.; Long, H.; Wang, K.; Wang, B.; Lu, P. Two-Photon-Pumped High-Quality, Single-Mode Vertical Cavity Lasing Based on Perovskite Monocrystalline Films. *Nano Energy* **2020**, *68*, 104334.
(22) Chen, S.; Zhang, C.; Lee, J.; Han, J.; Nurmikko, A. High-Q, Low-Threshold Monolithic Perovskite Thin-Film Vertical-Cavity Lasers. *Adv. Mater.* **2017**, *29*, 1604781.
(23) Zhang, Q.; Shang, Q.; Su, R.; Do, T. T. H.; Xiong, Q. Halide Perovskite Semiconductor Lasers: Materials, Cavity Design, and Low Threshold. *Nano Lett.* **2021**, *21*, 1903−1914.
(24) Lei, L.; Dong, Q.; Gundogdu, K.; So, F. Metal Halide Perovskites for Laser Applications. *Adv. Funct. Mater.* **2021**, *31*, 2010144.
(25) Zhang, L.; Yuan, F.; Dong, H.; Jiao, B.; Zhang, W.; Hou, X.; Wang, S.; Gong, Q.; Wu, Z. One-Step Co-Evaporation of All-Inorganic Perovskite Thin Films with Room-Temperature Ultralow Amplified Spontaneous Emission Threshold and Air Stability. *ACS Appl. Mater. Interfaces* **2018**, *10*, 40661−40671.
(26) Zhang, S.; Chen, J.; Shi, J.; Fu, L.; Du, W.; Sui, X.; Mi, Y.; Jia, Z.; Liu, F.; Shi, J.; et al. Trapped Exciton−Polariton Condensate by Spatial Confinement in a Perovskite Microcavity. *ACS Photonics* **2020**, *7*, 327−337.
(27) Hu, Y.; Bencheikh, F.; Chénais, S.; Forget, S.; Liu, X.; Adachi, C. High Performance Planar Microcavity Organic Semiconductor Lasers Based on Thermally Evaporated Top Distributed Bragg Reflector. *Appl. Phys. Lett.* **2020**, *117*, 153301.
(28) Wang, K.; Wang, S.; Xiao, S.; Zhang, N.; Wang, Y.; Yang, W.; Wang, Y.; Zhang, C.; Sun, W.; Song, Q. Single-Crystalline Perovskite Microlasers for High-Contrast and Sub-Diffraction Imaging. *Adv. Funct. Mater.* **2019**, *29*, 1904868.
(29) Tian, C.; Guo, T.; Zhao, S.; Zhai, W.; Ge, C.; Ran, G. Low-Threshold Room-Temperature Continuous-Wave Optical Lasing of Single-Crystalline Perovskite in a Distributed Reflector Microcavity. *RSC Adv.* **2019**, *9*, 35984−35989.
(30) Al Nakdali, D.; Shakfa, M. K.; Heinen, B.; Kunert, B.; Stolz, W.; Koch, S. W.; Hader, J.; Moloney, J. V.; Rahimi-Iman, A.; Koch, M. Analysis of Optical Scattering Losses in Vertical-External-Cavity Surface-Emitting Lasers. *Appl. Phys. B: Laser Opt.* **2015**, *120*, 41−46.
(31) Chen, S.; Nurmikko, A. Excitonic Gain and Laser Emission from Mixed-Cation Halide Perovskite Thin Films. *Optica* **2018**, *5*, 1141−1149.
(32) Zhang, H.; Hu, Y.; Wen, W.; Du, B.; Wu, L.; Chen, Y.; Feng, S.; Zou, C.; Shang, J.; Fan, H. J.; et al. Room-Temperature Continuous-Wave Vertical-Cavity Surface-Emitting Lasers Based on 2d Layered Organic−Inorganic Hybrid Perovskites. *APL Mater.* **2021**, *9*, 071106.
(33) Li, M.; Gao, Q.; Liu, P.; Liao, Q.; Zhang, H.; Yao, J.; Hu, W.; Wu, Y.; Fu, H. Amplified Spontaneous Emission Based on 2d Ruddlesden−Popper Perovskites. *Adv. Funct. Mater.* **2018**, *28*, 1707006.
(34) Liu, Z.; Hu, M.; Du, J.; Shi, T.; Wang, Z.; Zhang, Z.; Hu, Z.; Zhan, Z.; Chen, K.; Liu, W.; et al. Subwavelength-Polarized Quasi-Two-Dimensional Perovskite Single-Mode Nanolaser. *ACS Nano* **2021**, *15*, 6900−6908.
(35) Lin, J.; Hu, Y.; Liu, X. Microcavity Oleds: Microcavity-Enhanced Blue Organic Light-Emitting Diode for High-Quality Monochromatic Light Source with Nonquarterwave Structural Design. *Adv. Opt. Mater.* **2020**, *8*, 2070030.
(36) Lidzey, D. G.; Bradley, D. D. C.; Martin, S. J.; Pate, M. A. Pixelated Multicolor Microcavity Displays. *IEEE J. Sel. Top. Quant.* **1998**, *4*, 113−118.
(37) Zhang, H.; Zou, C.; Chen, Y.; Wu, L.; Wen, W.; Du, B.; Feng, S.; Shang, J.; Cong, C.; Yu, T. Continuous-Wave Vertical Cavity Surface-Emitting Lasers Based on Single Crystalline Lead Halide Perovskites. *Adv. Opt. Mater.* **2021**, *9*, 2001982.
(38) Wang, M.; Lin, J.; Hsiao, Y.-C.; Liu, X.; Hu, B. Investigating Underlying Mechanism in Spectral Narrowing Phenomenon Induced by Microcavity in Organic Light Emitting Diodes. *Nat. Commun.* **2019**, *10*, 1614.
(39) Guenther, K. H.; Wierer, P. G.; Bennett, J. M. Surface Roughness Measurements of Low-Scatter Mirrors and Roughness Standards. *Appl. Opt.* **1984**, *23*, 3820−3836.
(40) Zhang, D.; Fu, Y.; Liu, C.; Zhao, C.; Gao, X.; Zhang, J.; Guo, W.; Liu, J.; Qin, C.; Wang, L. Domain Controlling by Compound Additive toward Highly Efficient Quasi-2d Perovskite Light-Emitting Diodes. *Adv. Funct. Mater.* **2021**, *31*, 2103890.
(41) Xing, G.; Mathews, N.; Lim, S. S.; Yantara, N.; Liu, X.; Sabba, D.; Grätzel, M.; Mhaisalkar, S.; Sum, T. C. Low-Temperature Solution-Processed Wavelength-Tunable Perovskites for Lasing. *Nat. Mater.* **2014**, *13*, 476−480.
(42) Brenner, P.; Bar-On, O.; Jakoby, M.; Allegro, I.; Richards, B. S.; Paetzold, U. W.; Howard, I. A.; Scheuer, J.; Lemmer, U. Continuous Wave Amplified Spontaneous Emission in Phase-Stable Lead Halide Perovskites. *Nat. Commun.* **2019**, *10*, 988.
(43) Li, S.; Lei, D.; Ren, W.; Guo, X.; Wu, S.; Zhu, Y.; Rogach, A. L.; Chhowalla, M.; Jen, A. K. Y. Water-Resistant Perovskite Nanodots Enable Robust Two-Photon Lasing in Aqueous Environment. *Nat. Commun.* **2020**, *11*, 1192.
(44) Veldhuis, S. A.; Tay, Y. K. E.; Bruno, A.; Dintakurti, S. S. H.; Bhaumik, S.; Muduli, S. K.; Li, M.; Mathews, N.; Sum, T. C.; Mhaisalkar, S. G. Benzyl Alcohol-Treated Ch3nh3pbbr3 Nanocrystals Exhibiting High Luminescence, Stability, and Ultralow Amplified Spontaneous Emission Thresholds. *Nano Lett.* **2017**, *17*, 7424−7432.
(45) Grivas, C. Optically Pumped Planar Waveguide Lasers, Part I: Fundamentals and Fabrication Techniques. *Prog. Quant. Electron.* **2011**, *35*, 159−239.
(46) Wang, S.; Yu, J.; Zhang, M.; Chen, D.; Li, C.; Chen, R.; Jia, G.; Rogach, A. L.; Yang, X. Stable, Strongly Emitting Cesium Lead Bromide Perovskite Nanorods with High Optical Gain Enabled by an Intermediate Monomer Reservoir Synthetic Strategy. *Nano Lett.* **2019**, *19*, 6315−6322.
(47) Li, J.; Si, J.; Gan, L.; Liu, Y.; Ye, Z.; He, H. Simple Approach to Improving the Amplified Spontaneous Emission Properties of Perovskite Films. *ACS Appl. Mater. Interfaces* **2016**, *8*, 32978−32983.
(48) Chen, S.; Nurmikko, A. Stable Green Perovskite Vertical-Cavity Surface-Emitting Lasers on Rigid and Flexible Substrates. *ACS Photonics* **2017**, *4*, 2486−2494.
(49) Pourdavoud, N.; Haeger, T.; Mayer, A.; Cegielski, P. J.; Giesecke, A. L.; Heiderhoff, R.; Olthof, S.; Zaefferer, S.; Shutsko, I.; Henkel, A.; et al. Room-Temperature Stimulated Emission and Lasing in Recrystallized Cesium Lead Bromide Perovskite Thin Films. *Adv. Mater.* **2019**, *31*, 1903717.
(50) Zhai, W.; Tian, C.; Yuan, K.; Ge, C.; Zhao, S.; Yu, H.; Li, Y.; Chen, W.; Ran, G. Optically Pumped Lasing of Segregated Quasi-2d Perovskite Microcrystals in Vertical Microcavity at Room Temperature. *Appl. Phys. Lett.* **2019**, *114*, 131107.
(51) Tian, C.; Zhao, S.; Guo, T.; Xu, W.; Li, Y.; Ran, G. Deep-Blue Dbr Laser at Room Temperature from Single-Crystalline Perovskite Thin Film. *Opt. Mater.* **2020**, *107*, 110130.
(52) Bouteyre, P.; Nguyen, H. S.; Lauret, J.-S.; Trippé-Allard, G.; Delport, G.; Lédée, F.; Diab, H.; Belarouci, A.; Seassal, C.; Garrot, D.; et al. Room-Temperature Cavity Polaritons with 3d Hybrid Perovskite: Toward Large-Surface Polaritonic Devices. *ACS Photonics* **2019**, *6*, 1804−1811.

https://doi.org/10.1021/acs.jpclett.3c00279
J. Phys. Chem. Lett. 2023, 14, 2493−2500